RSC Advances

PAPER

View Article Online
View Journal | View Issue

Cite this: *RSC Adv.*, 2019, **9**, 1036

Metallic glassy Ti_2Ni grain-growth inhibitor powder for enhancing the hydrogenation/dehydrogenation kinetics of MgH_2

Mohamed Sherif El-Eskandarany *

Because of its high thermal stability and poor hydrogenation/dehydrogenation kinetics, magnesium hydride (MgH_2) requires mechanical treatment and/or doping with catalytic agents(s) to understand the decomposition temperature and accelerate the gas uptake/release kinetics. Whereas all catalytic species used for this purpose are crystalline materials, in this paper use of titanium nickel (Ti_2Ni) metallic glassy (MG) nanopowders for enhancing the hydrogenation/dehydrogenation kinetics behavior of MgH_2 powders is reported. In the present research, MG-Ti_2Ni ribbons, prepared using a melt spinning technique were snipped into small pieces and then cryo-milled under a flow of liquid nitrogen to obtain submicron-powders (500 nm). The as-prepared MgH_2 powders were doped with 10 wt% of the glassy powder and then cryo-milled for 25 h. The structural and morphological analysis indicated that the cryo-milling process succeeded in maintaining the short-range order structure of MG-Ti_2Ni, and in reducing the MgH_2 grain size to the nanolevel. The results showed that the as-prepared nanocomposite powders obtained after 25 h of cryo-milling decomposed at 283 °C, with an apparent activation energy of 87.3 kJ mol^{-1}. The MgH_2/10 wt% MG-Ti_2Ni nanocomposite powders were cold rolled into thin strips, using a cold rolling technique. These cold rolled strips possessed excellent morphological characteristics, shown by the homogeneous distribution of the MgH_2 spherical particles (10 nm in diameter) in the glassy Ti_2Ni matrix. Furthermore, the hydrogenation/dehydrogenation kinetics measured at 225 °C were very fast, as indicated by the short time (400 s) required to uptake/release 5.7 wt% H_2. At this temperature, the system possessed good life-time cycling performance – achieving 84 continuous cycles within 30 h without failure or degradation.

Received 3rd October 2018
Accepted 20th December 2018

DOI: 10.1039/c8ra08200f

rsc.li/rsc-advances

1. Introduction

Hydrogen (H_2) is an energy carrier which has tremendous promise for use as a new clean energy option in future energy systems.[1] Hydrogen storage, which cuts across both hydrogen production and hydrogen applications, and thus assumes a critical role in initiating hydrogen economy, has been the subject of intensive research for many years. However, hydrogen can be stored in compressed gas cylinders under very high pressure (~350 bar) or as a liquid at −253 °C, but using these storage approaches in real applications is difficult because of the high cost and safety issues.[1] Apart from such traditional ways of hydrogen storage, magnesium (Mg) and Mg-based materials have been considered as the most promising hydrogen storage materials.[2–4] The Mg-based alloys and nanocomposites have attracted worldwide interest of materials science, energy, and environmental scientists because of their light weight, capability to store a high volume of hydrogen[5] and the simplicity of mass production at ambient temperature, using reactive ball milling (RBM).[6,7]

Despite these attractive properties, magnesium hydride (MgH_2) in its pure form is very stable and has very slow hydrogenation/dehydrogenation kinetics at temperatures less than 350 °C.[8,9] Such serious drawbacks are considered as major barriers preventing the use of such an attractive metal hydride material for potential use in fuel cell applications.[10,11] Since the 1990s, enormous efforts have been dedicated for improving the hydrogenation/dehydrogenation behaviors of MgH_2, using pure metal catalysts,[12,13] intermetallic compounds,[14] metal oxides,[15,16] carbides[17] and different families of composite and nanocomposite materials.[18–21] Recently, Shinde *et al.*[22] demonstrated that successful self-assembly of MgH_2 nanoparticles in activated carbon led to the improvement of the physical and chemical behavior of the hydride phase for achieving reversible hydrogen storage.

In parallel, it has been indicated by several researchers that long-term ball milling leads to the formation of metastable γ-MgH_2 that possesses better hydrogenation/dehydrogenation kinetics when compared with the stable β-MgH_2 phase.[23,24] Sulaiman *et al.*[25] reported that MgH_2-*X* wt% potassium

Nanotechnology and Advanced Materials Program, Energy and Building Research Center, Kuwait Institute for Scientific Research, Safat 13109, Kuwait. E-mail: msherif@kisr.edu.kw

hexafluoronickelate(IV) (K_2NiF_6, $X = 5$, 10, 15, 20, and 50) nanocomposite systems showed fast hydrogenation/dehydrogenation kinetics with a low decomposition temperature. Yahya and Ismail have recently used a strontium titanate ($SrTiO_3$) compound to reduce the dehydrogenation temperature of MgH_2 to 275 °C.[26] Xiao *et al.* proposed milling MgH_2 powders with lithium chloride as an effective method for preparing MgH_2 containing a large mole fraction (18 wt%) of γ-MgH_2.[27] Using a carbon-wrapped transition metal [cobalt/carbon (Co/C), nickel/carbon (Ni/C)] nanoparticles was first proposed by Huang *et al.*, when they used this composite as a catalyst in MgH_2 system with ball milling to improve its de/rehydrogenation kinetics and to decrease the decomposition temperature.[28] It has been found that adding a small mole fraction (3 wt%) of another metal hydride system (titanium hydride, TiH_2) to MgH_2, leads to an enhancement of the kinetic behavior of MgH_2 and minimizes its decomposition temperature.[29] More recently, it has been demonstrated by Valentoni *et al.* that doping MgH_2 with vanadium niobium oxide ($VNbO_5$), a ternary oxide in the range 5, 10 and 15 wt%, leads to a significant reduction of the desorption temperature from 330 °C for the un-doped sample to 235 °C for the $VNbO_5$-doped sample.[30]

Apart from using crystalline (long-range order) materials for improving the behavior of MgH_2, in this paper the possibility of using short-range order (noncrystalline) titanium nickel (Ti_2Ni) for enhancing the uptake/release kinetics at low temperature, ranging from 150 °C to 225 °C, is reported. In addition, the performance of MgH_2 upon subjecting it to long-term charging/releasing long cycles was also investigated. In addition, the present research presents an interesting approach to fabricating a bulk MgH_2 nanocomposite system, using a simple method, which is used for the first time, as far as the author knows. The results are discussed from the point of view of structure, morphology, thermal stability, and kinetics.

2. Experimental methods

2.1 Sample preparation

2.1.1 MG-Ti_2Ni alloy nanopowders. Bulk metallic alloying elements of hexagonal close packed titanium (hcp-Ti) wires (99.99 wt%, 2 mm in diameter, Sigma-Aldrich # 348856), and face centered cubic nickel (fcc-Ni) wires (99.99% wt%, 2 mm in diameter, Sigma-Aldrich # GF17660594) were used as reactant materials. The materials were balanced to give a nominal composition of Ti_2Ni, etched with 70% water + 30% hydrochloric acid (Sigma-Aldrich # 320331) rinsed with ethanol (Sigma-Aldrich # 32205) and then dried at 200 °C in a drying oven for 3 h. An arc melter (AM 200, Edmund Bühler GmbH, Germany) was used in a zirconium (Zr)-gettered argon atmosphere to fabricate the desired Ti_2Ni alloy. A total weight of 100 g (66.67 g Ti and 33.33 g Ni) were placed layer by layer in a circular shaped groove of a water cooled copper (Cu) crucible. The arc melting process was started by melting the Zr getter and then melting the mixture of alloying elements. The metallic button obtained after melting was turned over and re-melted five times to ensure the homogeneity of fabricated alloy. The master alloy (Fig. 1a) was then removed from the arc melter, washed with acetone, ethanol and then crushed down into small pieces (~10 mm), using a 60 ton cold press. A representative small piece of the alloy was simply crushed into coarse powder (~120–180 μm in diameter) to examine its structure and composition, using X-ray diffraction (XRD) and inductively coupled plasma mass spectrometry, respectively. The results showed that the fabricated alloy had a fcc structure (space group *Fd3m*) with a lattice parameter, $a_o = 1.1278$ nm. Furthermore, the chemical composition of the sample examined was closed (66.83 wt% Ti and 33.17 wt% Ni) with a nominal composition (Ti-33.33 wt% Ni) of the starting materials. Metallic Ti_2Ni ribbons (Fig. 1b) were produced using a melt spinner-HV with a single Cu roller, with a boron nitride crucible.

The Cu wheel frequency was 70 Hz, where the difference of pressure for injection was 200 mbar. The distance from the crucible to the wheel was about 0.5 mm. The injection temperature was 1450 °C. The as-prepared Ti_2Ni ribbons were simply snipped into small pieces (~4–18 mm length), as shown in Fig. 1c.

For the purpose of the present research, 5 g of as-prepared snipped ribbons were sealed in chromium (Cr)-steel vial (80 ml in diameter) together with five Cr-steel balls (8 mm in diameter) under a helium (He) atmosphere in a glove box, using a ball-to-powder weight ratio of 10 to 1. The vial was then mounted on a cryo mill (Retsch, Germany). The cryo-milling process was operated under a continuous flow of liquid nitrogen with a constant milling frequency of 25 Hz (Fig. 1d). After 6 h of cryo-milling, the vial was released from the mill and opened in the glove box to discharge the milled composite powders.

2.1.2 MgH_2 powders. Elemental Mg metal powders (~80 μm, 99.8%, Sigma-Aldrich, # GF83190663), and hydrogen gas

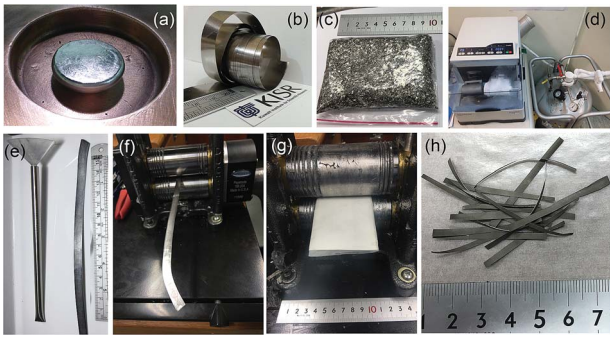

Fig. 1 Photographs presenting part of the experimental procedure used in this research for preparing bulk MgH_2/10 wt% α-Ti_2Ni nanocomposite strips. (a) Ti_2Ni master alloy prepared using the arc melting technique, (b) as-synthesized metallic glass (MG)-Ti_2Ni ribbons, using melt spinning, (c) small shots of as-prepared snipped MG-Ti_2Ni ribbons, and (d) a cryo-mill operated under a flow of liquid nitrogen. The as-prepared cryo-milled nanocomposite MgH_2/10 wt% α-Ti_2Ni nanocomposite powders obtained after 25 h were charged into a stainless steel tube through a plastic funnel (e) and then cold rolled for 10 passes (f). The tube was then opened in the glove box to take out the cold rolled strips, which were straightened using cold rolling for 30 passes (g), to obtain straight strips 6.5–7 cm length (h).

(99.999 wt%) were used as starting materials. A portion of 5 g of Mg was balanced inside a He gas atmosphere (99.99 wt%) in a glove box. The powders were then sealed together using 50 hardened steel balls in a hardened steel vial (220 ml in volume), using a gas-temperature monitoring system (evico magnetics, Germany). The ball-to-powder weight ratio was 40 : 1. The vial was then evacuated to a pressure of 10^{-3} bar before introducing H_2 gas to fill the vial to a pressure of 50 bar. The RBM process was carried out at room temperature, using a high energy ball mill (Planetary Mono Mill PULVERISETTE 6, Fritsch, Germany). After 6 h of RBM, the powders were discharged from the vial inside the glove box and sealed in two Pyrex vials.

2.1.3 MgH_2/10 wt% Ti_2Ni nanocomposite powders. The as-synthesized MgH_2 powders were mixed in the glove box with 10 wt% of cryo-milled Ti_2Ni MG-powders, using an agate mortar and pestle. The mixed powders were then charged together using five Cr-steel balls in a Cr-steel vial and sealed under a He gas atmosphere. The system was mounted on the cryo-mill operated under a flow of liquid nitrogen for 25 h.

2.1.4 Bulk MgH_2/10 wt% Ti_2Ni nanocomposite strips. Nanocomposite MgH_2/10 wt% MG-Ti_2Ni powders obtained after 25 h of cryo-milling were charged and sealed in a stainless steel (SUS304) tube (0.8 cm diameter and 20 cm length) inside the glove box (Fig. 1e). The system was then cryomilled at room temperature, using a two drum type manual cold roller (11 cm wide $\times$ 5.5 cm diameter rollers), as shown in Fig. 1f.

The deformed tube obtained after 30 passes was opened in the glove box, where the cryo-milled materials were removed. The cold rolling process led to the formation of short strips, with irregular edges and lengths. The strips were trimmed to have near net lengths of $\sim$6.5 cm, when the crumbled irregular edges were cut away. This process was repeated 10 times in order to obtain 30 g. The strips were then placed between two SUS304 sheets and gently cryo-milled 10 times (Fig. 1g) to ensure the weldability of the MgH_2 particles with the amorphous matrix of Ti_2Ni. Fig. 1h presents the typical final product of cryo-milled nanocomposite strips prepared in this present study.

2.2 Sample characterizations

2.2.1 Crystal structure. The crystal structure of all the prepared samples was investigated using X-ray diffraction (XRD) with CuKα radiation, using a 9 kW SmartLab intelligent X-ray diffraction system (Rigaku, Japan). The local structure of the synthesized material was investigated using a JEM-2100F 200 kV field emission high resolution transmission electron microscopy/scanning transmission electron microscopy (HRTEM/STEM, Jeol Japan), equipped for energy-dispersive X-ray spectroscopy (EDS, Oxford Instruments, UK).

2.2.2 Thermal analysis. A differential scanning calorimetry (DSC) system (Setaram, France) with a heating rate of 10 °C min^{-1} was used to investigate the glass transition temperature (T_g), and crystallization temperature (T_x) for the MG-Ti_2Ni ribbons. A Thermal Analysis Workstation System (TA-60WS, Shimadzu), using DSC was used to investigate the decomposition temperature (T_{deo}) of the MgH_2-composites, with a heating rate of 10 °C min^{-1}. The apparent activation energy (E_a) for the synthesized MgH_2-composites was investigated, using the Arrhenius approach with different heating rates of 5, 10, 20, and 40 °C min^{-1}.

3. Results

Fig. 2a displays the bXRD pattern of the fcc-Ti_2Ni master alloy button (Fig. 1a) prepared using the arc melting technique. The sharp Bragg peaks indexed in Fig. 2a are well matched with those of the fcc-Ti_2Ni (PDF file # 00-018-0898). Fig. 2b shows the XRD pattern of Ti_2Ni ribbons (Fig. 1b) prepared by melt spinning the Ti_2Ni alloy button. Obviously, all the Bragg peaks related to the fcc-Ti_2Ni phase had disappeared and been replaced by broad diffuse halos, indicating the formation of the Ti_2Ni amorphous phase, as shown in Fig. 2b.

The HRTEM image of the as-prepared ion sliced Ti_2Ni ribbon is shown in Fig. 3a together with the corresponding selected area diffraction (SAED) pattern. The image revealed a homogeneous structure with maze-like contrast without contrast related to precipitations of any crystalline phases (Fig. 3a). Furthermore, the SAED pattern displayed the typical halo-diffraction of an amorphous phase, as presented in Fig. 3b. The absence of sharp

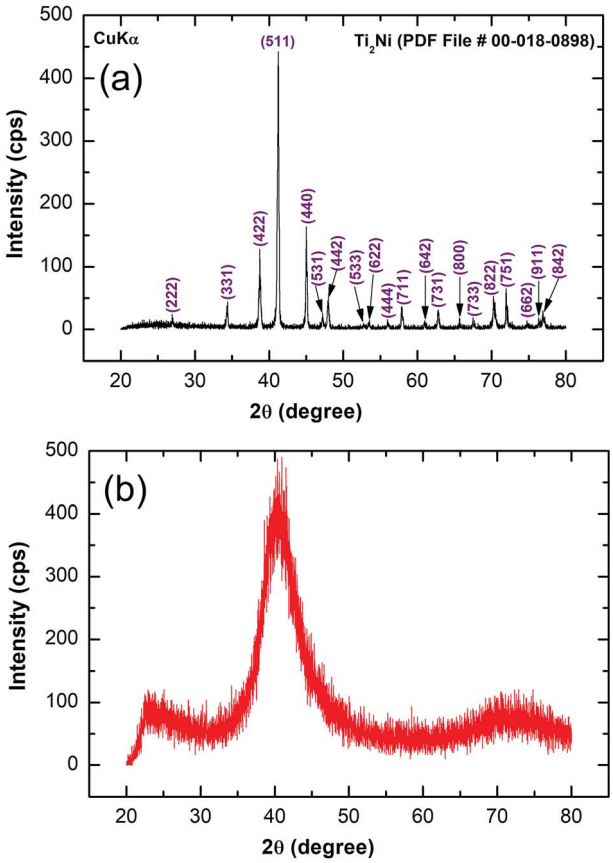

Fig. 2 XRD patterns of (a) Ti_2Ni master alloy obtained after the arc melting process, and (b) amorphous Ti_2Ni ribbon synthesized using a melt spinning approach. The diffuse halo pattern shown in (b) indicates the formation of an amorphous phase.

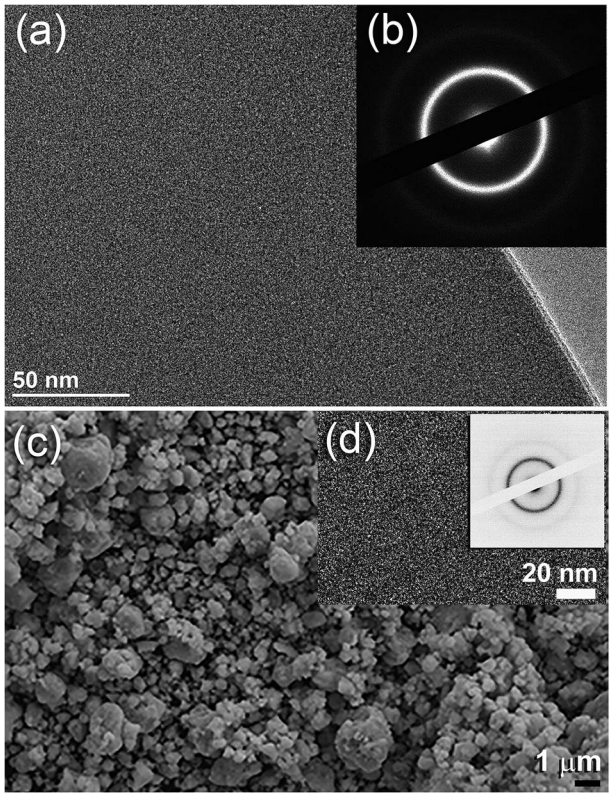

Fig. 3 (a) HRTEM image of Ti_2Ni ribbon synthesized using the melt spinning approach, and (b) SAED pattern taken in the middle zone of (a). (c) FE-SEM micrograph of as-prepared snipped ribbons cryo-milled for 6 h. The HRTEM and corresponding NBDP of cryo-milled Ti_2Ni powders are shown together in (d).

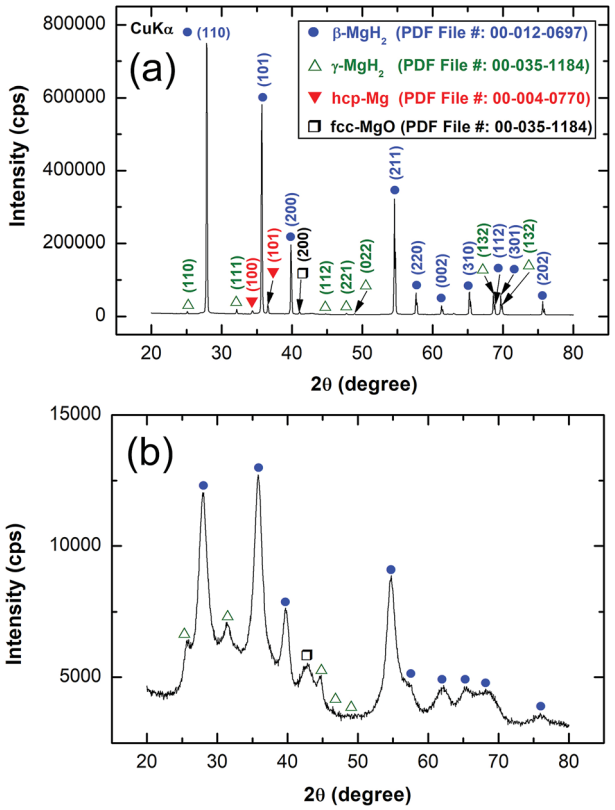

Fig. 4 XRD patterns of the as-prepared (a) MgH_2 powders, obtained after 6 h of RBM, and (b) nanocomposite MgH_2/10 wt% MG-Ti_2Ni powders obtained after 25 h of cryo-milling time.

rings and/or spots indicated the absence of any unprocessed Ti_2Ni crystalline phase in the prepared amorphous ribbons.

The field effect-scanning electron (FE-SEM) micrograph of the snipped Ti_2Ni ribbons (Fig. 1c) cryo-milled for 6 h under a flow of liquid nitrogen (Fig. 1d) is presented in Fig. 3c. The amorphous powders obtained after this stage of milling possessed spherical-like morphology with a particle size distribution in the range of 0.5 μm to 3 μm in diameter, as displayed in Fig. 3(d). It should be emphasised that the cryo-milling process was able to maintain the short-range order of α-Ti_2Ni ribbons without crystallization. This is shown by the featureless morphology of the amorphous powders (Fig. 3d) and the presence of a halo electron diffraction pattern (inset of Fig. 3d).

The XRD pattern of MgH_2 powders obtained upon reactive ball RBM of hcp-Mg powders under 50 bar pressure of H_2 for 6 h is displayed in Fig. 4(a). Pronounced sharp Bragg peaks corresponding to β-MgH_2 phase (PDF file # 00-012-0697) co-existed with a small volume fraction of metastable γ-MgH_2 phase[31] presented together with marginal fraction of unreacted hcp-Mg phase (PDF file # 00-004-0770), as shown in Fig. 4a. At this stage of RBM, the major β-MgH_2 phase consisted of large equiaxed grains with a grain size distribution lying in the range of 35 nm to 98 nm, as presented in Fig. 5a. The fast Fourier transform (FFT) image of Zone I oriented to [001] confirmed the formation of β-MgH_2, as shown in Fig. 5b.

The XRD pattern of MgH_2 doped with 10 wt% of MG-Ti_2Ni powders and then cryo-milled for 25 h is presented in Fig. 4b. It was plainly seen that the Bragg peaks related to β-MgH_2 became broad and had a lower intensity when compared with the corresponding diffraction lines shown in Fig. 4a, implying the

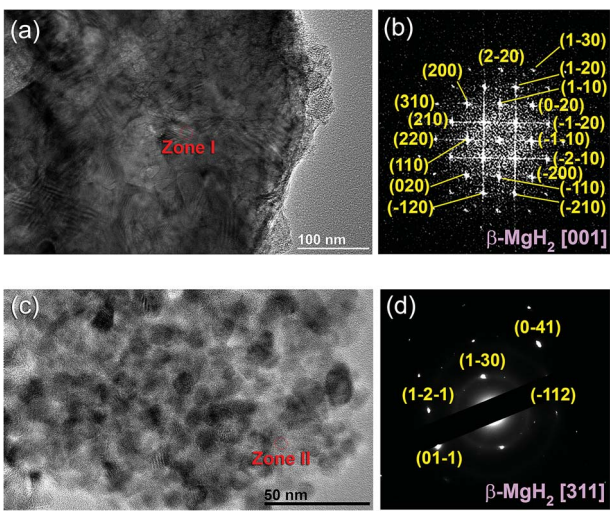

Fig. 5 HRTEM and FFT images of MgH_2 powders are presented in (a and b), where the HRTEM and NBDP images corresponding to the nanocomposite MgH_2/10 wt% MG-Ti_2Ni powders are displayed in (c) and (d), respectively.

formation of ultrafine MgH_2 powders after short cryo-milling time (25 h). It should be emphasised that particle size refinement was conducted upon ball milling with hard spherical MG-Ti_2Ni powders, which acted as micro/nano milling media. It is also worth noting the absence of diffracted lines related to the crystalline fcc-Ti_2Ni phase. This implies that the cryo-milling step maintained the short range order of Ti_2Ni without crystallization. The Bragg peaks of β-MgH_2 lines were overlapped with a diffuse halo pattern relating to the MG-Ti_2Ni phase (Fig. 4d), suggesting that nanocomposite powders had been formed.

The FE-HRTEM image and the corresponding nanobeam diffraction pattern (NBDP) of the nanocomposite MgH_2/10 wt% MG-Ti_2Ni powders obtained after 25 h of cryo-milling are displayed in Fig. 5c and d, respectively. The cryo-milled powders consisted of a fine featureless light-grey matrix hosting segregated dark grey particles (Fig. 5c) having an average diameter size of 9 nm. The NBD of a crystalline zone (Zone II) oriented to [311] confirmed the presence of a crystalline β-MgH_2 phase overlapped with the first and second halo rings of the MG-Ti_2Ni phase (Fig. 5d).

The thermal stabilities of MG-Ti_2Ni, MgH_2, and nanocomposite MgH_2/10 wt% MG-Ti_2Ni powders were examined, using DSC. The DSC curve obtained at a heating rate of 10 °C min^{-1} of the as-prepared cryomilled MG-Ti_2Ni powders revealed two opposite events, as shown in Fig. 6a. The first was an endothermic reaction which happened because of a glass transformation reaction at an onset temperature (T_g) of 467 °C, as shown in Fig. 6b. The T_g, which referred to the solid amorphous–liquid amorphous phase transformation, was followed by a single sharp exothermic reaction achieved at an onset temperature of 549 °C (Fig. 6b).

The XRD pattern of the sample heated up to 735 °C in the DSC (not shown here) revealed Bragg peaks corresponding to the fcc-Ti_2Ni crystalline phase. This implied that the exothermic peak shown in Fig. 6(a) was related to the crystallization of the MG-Ti_2Ni phase at a T_x of 569 °C (Fig. 6a). This binary MG system shows a rather wide supercooled liquid region ($\Delta T_x = T_x - T_g$) extended to 82 °C, as displayed in Fig. 6b.

In order to avoid undesired pre-and/or crystallization of the MG-Ti_2Ni phase, the maximum applied DSC temperature was 400 °C, which was far below the T_x. Each measurement revealed single endothermic decomposition reaction peaks which appeared at different peak temperatures, as presented in Fig. 6d. The E_a calculation, based on an Arrhenius approach, showed a lower value (87.3 kJ mol^{-1}) when compared with the corresponding E_a of MgH_2 powders obtained after 6 h of RBM (141.6 kJ mol^{-1}).

The HRTEM image of MgH_2/10 wt% MG-Ti_2Ni powders milled for 25 h and heated up to 400 °C in DSC is displayed in Fig. 7a. The sample consisted of nanoparticle (~5 nm to 20 nm in diameter) embedded in a fine featureless matrix. The atomic resolution TEM image taken from the indexed red zone shown in Fig. 7a is presented together with the corresponding NBDP shown in the inset of Fig. 7b. The TEM image revealed a moiré fringe image corresponding to interplanar spacing, $d = 0.2439$ nm for Mg(100). The NBDP shown in Fig. 7b revealed bright spots related to the hcp-Mg crystal oriented to the zone axis [111]. These spots were clearly overlapped with the first and second halo rings of MG-Ti_2Ni, as shown in Fig. 7b. Based on the current TEM resolution, neither MgH_2 nor fcc-Ti_2Ni could be detected for the sample heated up to 400 °C. This suggests full decomposition of the MgH_2 phase, where the MG-Ti_2Ni matrix maintained its original amorphous structure without crystallization.

Fig. 8(a) displays the bright field image (BFI) of the cross-sectional view for an ion-sliced MgH_2/10 wt% MG-Ti_2Ni nanocomposite sheet obtained after the cold rolling process (Fig. 1h). The cold rolled material showed excellent morphological characterization, indicated by the segregation of MgH_2 particles that had uniform spherical shapes and narrow particle size distribution (~10 nm in diameter, Fig. 8a). As a result of the cold rolling process, the MgH_2 powders were deeply embedded into the fine amorphous matrix to form a typical nanocomposite system, as displayed in Fig. 8a.

The XRD pattern related to nanocomposite strip sample is presented in Fig. 8b. The sample revealed a diffuse halo pattern related to the MG-Ti_2Ni phase, which co-existed with broad and low intensity Bragg peaks corresponding to β- and γ-MgH_2 phases, as shown in Fig. 8b. The absence of a crystalline phase related to fcc-Ti_2Ni may suggest the capability of the MG-Ti_2Ni matrix to withstand the mechanical imperfections introduced by the cryo-milling process. In addition, the significant reduction in MgH_2 particle size resulted because of the powder disintegration which the particle underwent with the cryo-milling process.

To investigate the degree of homogeneity and elemental distribution for the cryo-milled strip sample, an STEM/EDS

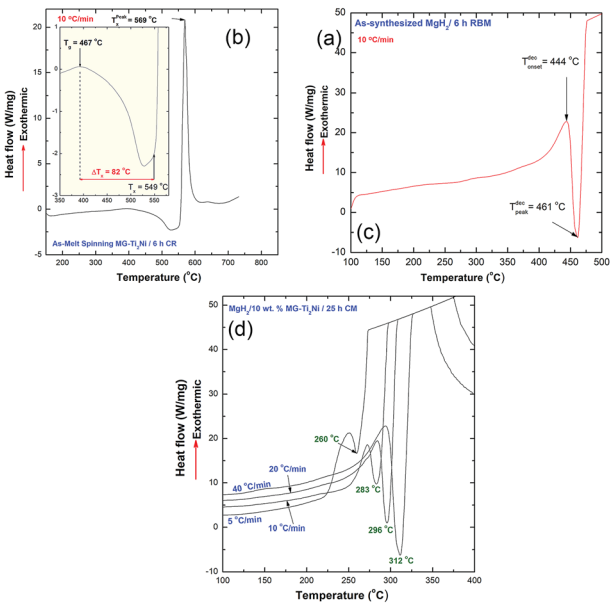

Fig. 6 (a) DSC curve of the as-prepared MG-Ti_2Ni powders obtained after 6 h of cryo-milling. The glass transition region shown in (a) is also presented in (b) using a different scale. The DSC curve of the as prepared MgH_2 powders, obtained after 6 h of RBM is displayed in (c), whereas the DSC curves obtained at different heating rates for nanocomposite MgH_2/10 wt% MG-Ti_2Ni powders obtained after 25 h of cryo-milling are presented in (d).

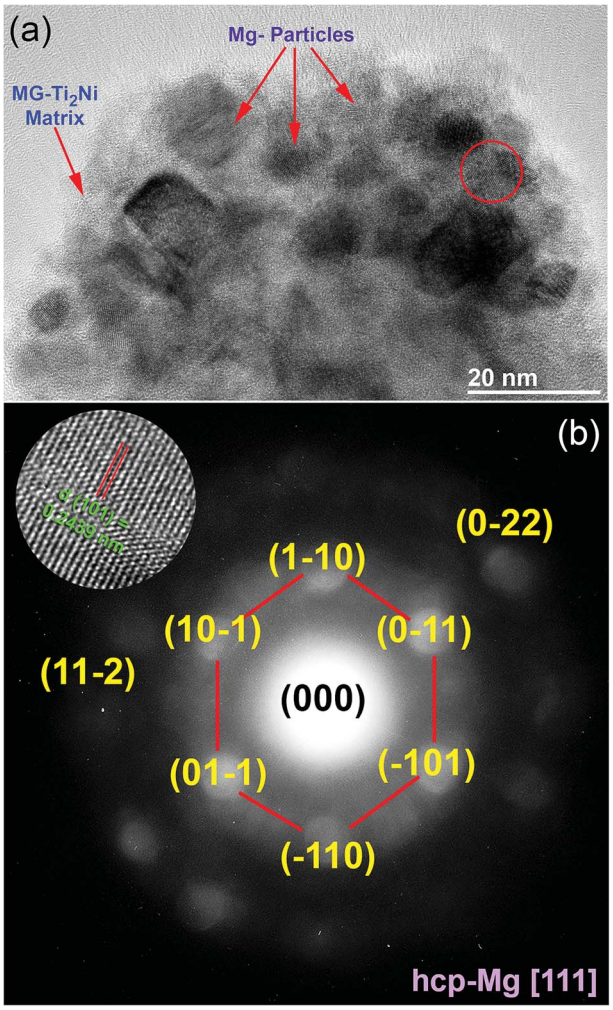

Fig. 7 HRTEM and NBDP images for nanocomposite sample taken after a DSC experiment operated at 10 °C min^{-1} are shown in (a) and (b), respectively.

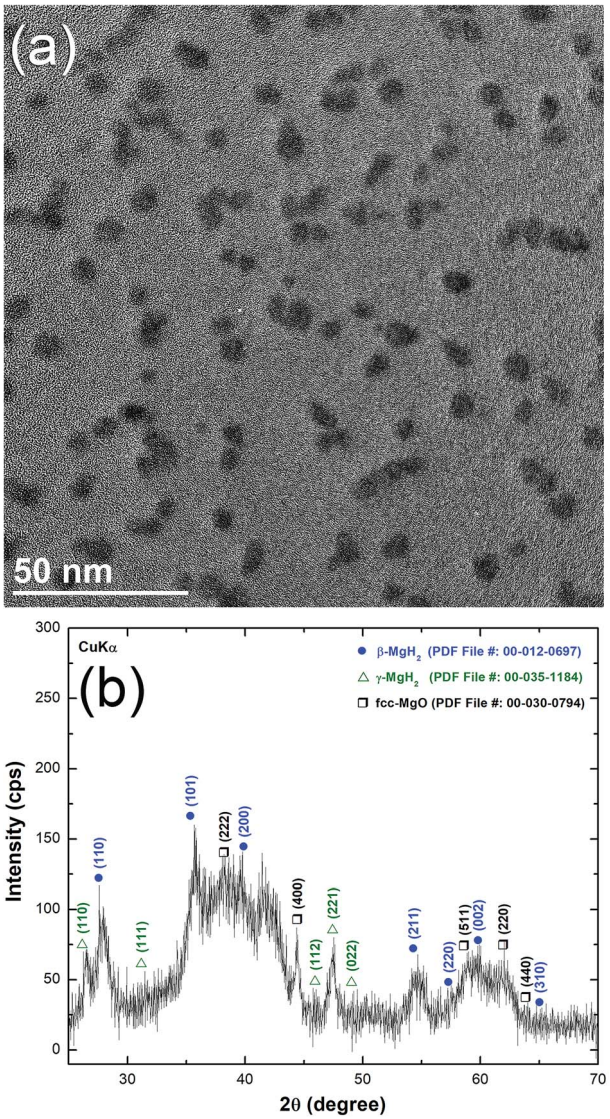

Fig. 8 (a) BFI of cross-sectional view for an ion-sliced nanocomposite strip sample after the cryo-milling process, and (b) the corresponding XRD pattern. The nanosized lenses presented in (a) refer to MgH_2 particles embedded into MG-Ti_2Ni matrix (grey matrix).

approach was used. The STEM/dark field image (DFI) of the cold rolled strip sample consisted of nanocrystalline grains with an average particle diameter size of 6.8 nm as shown in Fig. 9a. These spherical-like grains were related to MgH_2 powders, as indicated by the EDS-mapping of Mg-Kα_{1-2} (Fig. 9b). The EDS-mapping for the alloying elements (Ti and Ni) of the amorphous matrix were fairly distributed over the whole matrix without compositional fluctuations or degradation, as shown in Fig. 9c and d. This showed that the chemical composition uniformity of α-Ti_2Ni was beyond the nanoscale level. The average EDS compositional analysis taken from 25 individual zones, using a 5 nm beam diameter for Mg, Ti and Ni elements was 90.85 wt% Mg and 9.15 wt% Ti_2Ni. This value was very close to the nominal composition of the starting material MgH_2/10 wt% MG-Ti_2Ni.

Fig. 10a presents the hydrogenation kinetics of the cold rolled strip conducted at different temperatures under 10 bar of H_2. At low temperatures of 150 °C, and 175 °C, the sample absorbed about 3.5 and 4.8 wt% of H_2, respectively, within 100 s, as shown in Fig. 10a. At a medium temperature range of 200 °C and 225 °C, the hydrogen concentrations absorbed after 100 s were 4.9 and 5.1 wt% H_2, respectively. The amount of hydrogen absorbed for the samples examined at 150 °C after 300 s was 4.9 wt% (Fig. 10a). This value increased monotonically with increase of the applied absorption time and tended to become saturated at 5.5 wt% after 479 s, as shown in Fig. 10a.

The sample measured at 175 °C showed better hydrogenation kinetics, as indicated by the shorter time (444 s) required to absorb 5.5 wt% H_2. A moderate improvement on the hydrogenation kinetics was attained for the sample measured at 200 °C, as suggested by the short time (356 s) necessary to upload 5.5 wt% H_2 (Fig. 10a).

At 225 °C, the sample had significant fast absorption kinetics, characterized by the very short time (194 s) required to upload 5.5 wt% H_2. Increasing the absorption time to 400 s

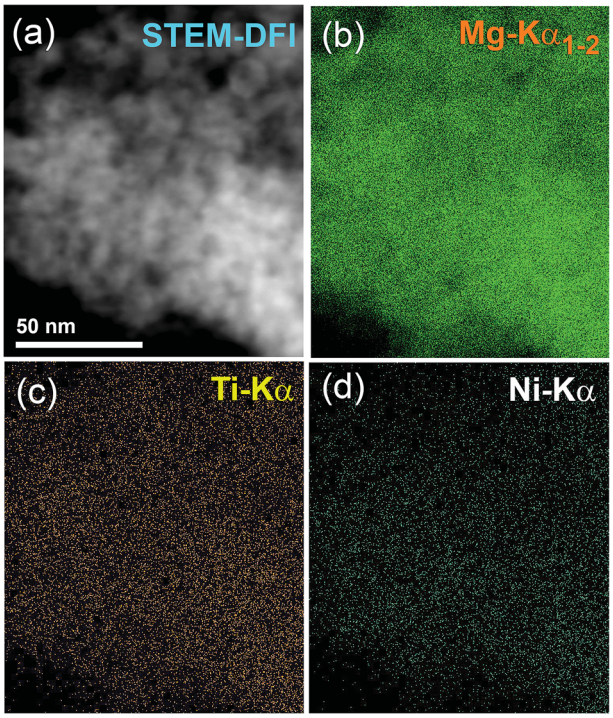

Fig. 9 STEM-DFI of nanocomposite strip sample is displayed in (a) together with EDS-elemental mapping for (b) MgKα_{1-2}, (c) Ti-Kα, and (d) Ni-Kα.

allowed the sample to absorb a greater amount of hydrogen (5.7 wt% H_2), where it became saturated at this value with a longer absorption time (500 s), as shown in Fig. 10a.

The STEM image and XRD pattern of the sample obtained after a hydrogenation time of 500 s at 225 °C, are shown in Fig. 10b and c, respectively. The hydrogenated sample possessed a typical nanostructure, characterized by the presence of spherical nanoparticles (~11–20 nm in diameter) embedded in an MG-Ti_2Ni fine matrix as shown in Fig. 10b. The XRD pattern of the as-prepared hydrogenated sample revealed Bragg peaks corresponding to β- and γ-MgH_2 phases co-existing with unprocessed hcp-Mg (Fig. 10c).

The dehydrogenation kinetic behavior of cold rolled MgH_2/10 wt% α-Ti_2Ni nanocomposite strips was examined under 200 mbar H_2 at three different temperatures. The sample measured at a low temperature (175 °C) showed poor dehydrogenation kinetics, characterized by a very long time (1331 s) taken to desorb −3 wt% H_2 (Fig. 10d). This sample required a desorption time of 3611 s to release −5.2 wt% H_2, as indicated in Fig. 10d. In contrast to this, the sample measured at a moderate temperature of 200 °C possessed very fast dehydrogenation kinetics, shown by the very short time (353 s) taken to release −3 wt% H_2 (Fig. 10d).

After only 922 s, the sample was able to release −5.5 wt% H_2. No remarkable change in the amount of released H_2 could be obtained even after processing for 2411 s, suggesting completion of desorption process, as shown in Fig. 10d. Superior

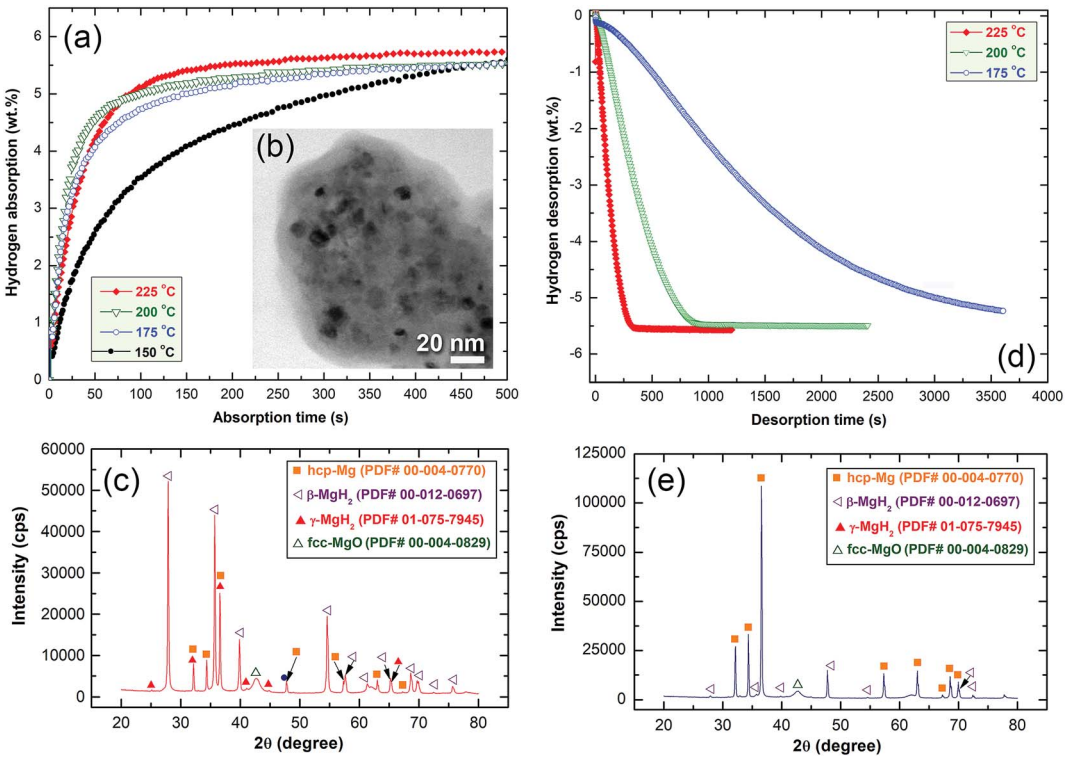

Fig. 10 (a) Hydrogenation kinetics of nanocomposite MgH_2/10 wt% α-Ti_2Ni strip samples measured at 150, 175, 200 and 225 °C/10 bar, using Sievert's method. (b) BFI of the sample examined at 225 °C, displaying MgH_2 powder particles embedded in the α-Ti_2Ni matrix. (c) Corresponding XRD patterns of the sample hydrogenated at 225 °C. (d) Dehydrogenation experimental results conducted at 175, 200, 225 °C/200 mbar nanocomposite MgH_2/10 wt% α-Ti_2Ni strip samples. (e) XRD pattern of dehydrogenated sample at 225 °C.

dehydrogenation kinetics was obtained with a small increase of the desorption temperature to 225 °C. At this temperature, the sample was able to desorb −3 wt% H_2 in a very short time (105 s), as displayed in Fig. 10d. Increasing the time to 333 s caused the sample to desorb its full hydrogen storage capacity (−5.7 wt% H_2), where there was no remarkable change in this value even if a longer desorption time (1224 s) was used, as shown in Fig. 10d.

Fig. 10(e) presents the XRD pattern of the sample heated at 225 °C and taken after complete release of H_2. The sample revealed very sharp Bragg peaks related to the hcp-Mg overlap with minor diffraction lines from the undecomposed β-MgH_2 phase, as shown in Fig. 10e.

The cycle-life-time test is one of the most important and fundamental characterization approaches used to examine the performance of metal hydrides. In the present study, the cold-rolled strip nanocomposite was examined at 225 °C under H_2 pressures varying from 200 mbar (desorption) to 10 bar (absorption). The test was repeated in a cyclic fashion for 30 h, and the results are shown in Fig. 11a. In order to maintain the short-range order of the MG-Ti_2Ni matrix and to avoid its potential crystallization, the nanocomposite strip was not activated. The sample shows good cyclic performance, characterized by the near hydrogen storage values (5.48 wt% H_2) and closed uptake/release kinetics during the cycle-life-time extended to 30 h (Fig. 11a).

The low magnification BFI of the sample taken after the cycle-life-test is shown in Fig. 11b. Obviously, the Mg particles obtained after the cycle test were segregated and maintained their nano spherical-like morphology (~9 nm in diameter), as shown in Fig. 11b. Furthermore, they were uniformly embedded in the matrix, which indicated the homogeneity of chemical composition. The corresponding SAED pattern exhibited primary and secondary haloes related to the MG-Ti_2Ni phase (matrix), as shown in Fig. 11c. These haloes overlapped with sharp spots (Fig. 11c) corresponding to the Mg crystals embedded in the matrix with different orientations. A pressure–composition–temperature (PCT) test was used to examine the cyclability and performance of pure MgH_2 powders obtained after 6 h of RBM.

The PCT experiment was conducted at 300 °C under 70 bar of H_2 pressure for 100 continuous cycles, as shown in Fig. 11d. However, the first cycle, showed a high H_2 storage capacity of 6.8 wt%, and the following cycles (2 to 100) revealed a seriously steep degradation of this value (Fig. 11d). After 50 cycles, the hydrogen storage capacity decreased to 5.7 wt%, where it then decreased to 5.3 wt% after processing for 100 cycles, as shown in Fig. 11d.

The morphological characteristics of the MgH_2 sample obtained after processing for 100 cycles in the PCT test were investigated using TEM analysis (Fig. 11e). The sample revealed a single phase of Mg metal, as indicated by the sharp spots corresponding to Mg[023] presented in Fig. 11f. The Mg metal obtained after the PCT test suffered from an extreme agglomeration effect, which resulted in a formation of very large powder particles with an apparent size of 10 μm, as shown in Fig. 11e.

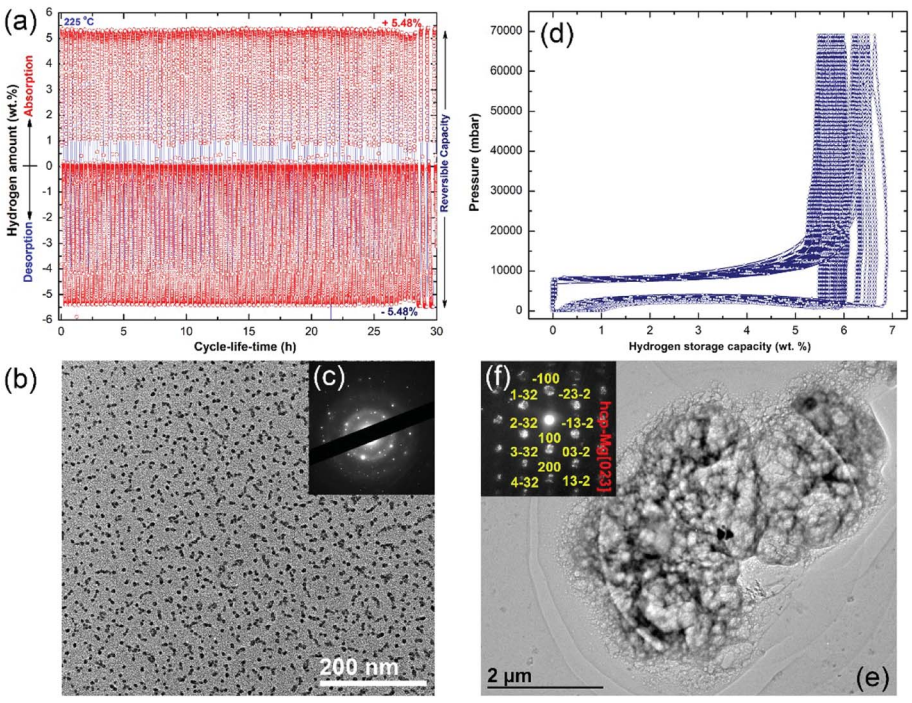

Fig. 11 (a) Hydrogenation/dehydrogenation cycle-life-time test of nanocomposite MgH_2/10 wt% MG-Ti_2Ni strip samples, conducted at 225 °C under 10 bar (uptake) and 200 mbar (release) to cover 84 continuous cycles within 30 h. (c) BFI and (c) corresponding NBDP of the sample after completion of 84 cycles. For comparison, the PCT/cycle-life-time test of pure MgH_2 obtained after 6 h of RBM is displayed in (d). A low magnification BFI image of pure MgH_2 after complete of PCT test is presented together with related NBDP in (e) and (f), respectively.

4. Discussion

The present paper proposes a new approach for the fabrication of bulk nanocomposite MgH_2/10 wt% MG-Ti_2Ni strips, using multi-techniques. The MG-Ti_2Ni nanopowders played an important role as hard abrasive powders for refining the MgH_2 microscaled-powders obtained after 6 h of RBM (Fig. 12a). During the cryo-milling process, the MG-Ti_2Ni adhered to the surface of MgH_2 powders to act as micro-milling media (Fig. 12b). The ball-powder-ball collisions resulted in the refinement of the hard MG powders giving them a large surface area. Increasing the cryo-milling time caused the spherical MG-Ti_2Ni powders to be embedded into the MgH_2 powders (Fig. 12c).

During the last stage of milling, the MgH_2 powder sizes reached a level (less than 1 μm in diameter) in which the ball-milling media could not introduce effective "trap and nipping" of the powders, which are required for further grain refining. Increasing the ball milling time led also to the "migration" of a large volume fraction of the abrasive MG powders through the cavities and micro-channels created in the body of the MgH_2 particles to be located close to the grains. Thus, they broke up the large MgH_2 grains (Fig. 12c) along their weak grain boundary zones (Fig. 12d) to form finer powders with a large volume fraction of nanostructured MgH_2 grains co-existing with the MG-Ti_2Ni particles (Fig. 12e).

It was found that the cold rolling of cryo-milled nanocomposite powders for 30 passes (Fig. 12f) had a beneficial effect on achieving further grain refining of the MgH_2 powder upon the introduction of severe plastic deformation on the MgH_2 grains.

In addition, this led to the consolidation of the powders into bulk nanocomposite strips with a good distribution of MgH_2 powders into the noncrystalline MG powder-matrix (Fig. 12g). Because the H_2 diffusion is much faster along the grain boundaries when compared with grains inside, the hydrogenation/dehydrogenation kinetic behaviors of MgH_2 were gradually improved with increase of the number of "liberated" grains.

Table 1 summarizes the results of H_2 storage properties obtained in the present work in comparison with some of other systems. For this purpose, abrasive catalytic powders, such as metal oxides, carbides and intermetallic compounds were chosen. As is clearly shown from the results shown in Table 1, the hydrogenation/dehydrogenation kinetics of the present system is very fast when compared, for example, with metal oxides [10 wt% niobium(v) oxide (Nb_2O_5), aluminium oxide (Al_2O_3) and silicon carbide (SiC)]. Whereas the gas uptake and release of the present system were achieved at a rather low temperature (225 °C), higher temperatures were always required for most of the other systems, as shown in Table 1. However, the results of a recent study[34] showed that a MgH_2/10 wt% Nb_2O_5 system possessed very fast hydrogenation and dehydrogenation kinetics for absorption/desorption of 5 wt% H_2 at 225 °C within 1200 s/700 s.

It has recently been found that the MgH_2/15 wt% vanadium niobium oxide ($VNbO_5$) system possessed excellent kinetics behavior.[37] This was indicated by the low temperature (160 °C)

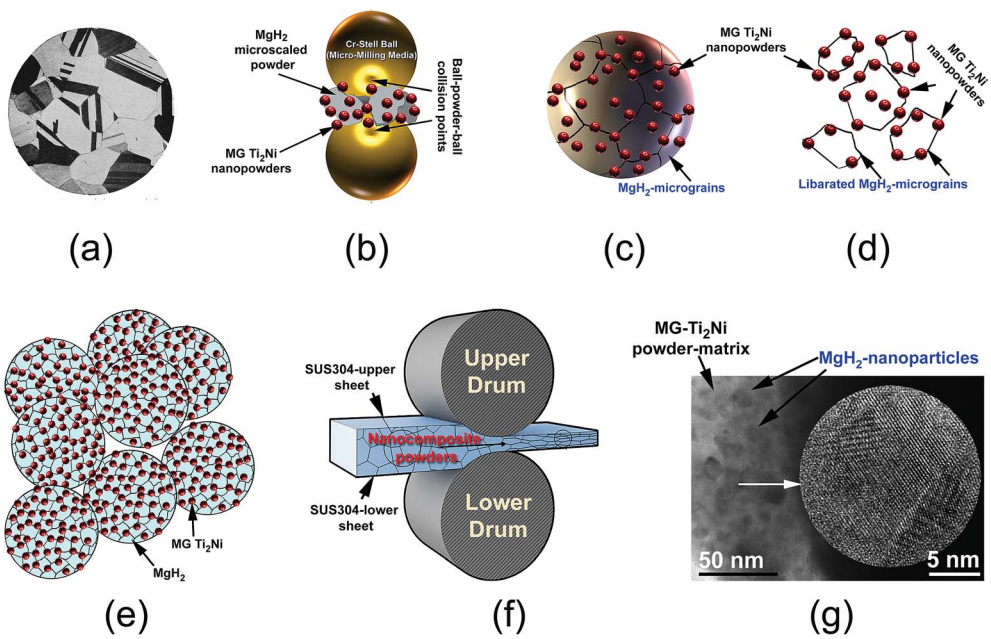

Fig. 12 Schematic diagram showing the mechanism of forming the nanocomposite MgH_2/10 wt% MG-Ti_2Ni powders. (a) Optical microscope micrograph of polished MgH_2 powders obtained after 6 h of RBM. A schematic presentation showing the ball-powder-ball collision taking place during the cryo-milling process of MgH_2-10 wt% MG-Ti_2Ni powders (b), adhesion of MG-Ti_2Ni powders on the surface of MgH_2 powder particle (c), disintegration the large MgH_2 grains during the cryo milling process (d), formation of nanocomposite fine powders (e), and (f) cold rolling process of the nanocomposite MgH_2/10 wt% MG-Ti_2Ni powders. The BFI and FE-HRTEM of the bulk nanocomposite strip obtained after cold rolling are shown together in (g).

Table 1 Hydrogen storage properties of ball milled MgH_2 powders doped with abrasive powders of selected metal oxides, carbides and intermetallic compounds

Catalyst	Hydrogenation/dehydrogenation properties	Ref.
10 wt% MG-Ti_2Ni	Absorption/5.7 wt% H_2/10 bar/225 °C/400 s, desorption/5.7 wt% H_2/200 mbar/225 °C/400 s, cycle-life-time: 30 h (84 cycles)	Present work
5 wt% Nb_2O_5	Absorption/5.2 wt% H_2/10 bar/300 °C/400 s,dDesorption/6 wt% H_2/0.1 kPa/300 °C/400 s	32
10 wt% Nb_2O_5	Absorption/5.8 wt% H_2/5 bar/300 °C/30 min, desorption/5.8 wt% H_2/0.1 bar/300 °C/350 min	33
10 wt% Nb_2O_5	Absorption/5.0 wt% H_2/10 bar/225 °C/1200 s, desorption/5.0 wt% H_2/0.02 bar/225 °C/700 s	34
10 wt% Al_2O_3	Absorption/4.09 wt% H_2/15 bar/300 °C/110 min, desorption/NA	35
10 wt% Al_2O_3	Absorption/4.22 wt% H_2/12 bar/320 °C/10 min/max storage capacity: 5.2 wt%, desorption/NA	36
15 wt% $VNbO_5$	Absorption/5.5 wt% H_2/20 bar/160 °C/10 min, absorption/desorption 50 cycles/275 °C	37
10 wt% SiC	Absorption/3.7 wt% H_2/10 bar/350 °C/140 s, desorption/2.5 wt% H_2/0.02 bar/350 °C/2000 s	38
10 wt% $V_{0.75}Ti_{0.05}Cr_{0.20}$	Absorption/3 wt% H_2/1 bar/25 °C/75 min/max storage capacity: 6.1 wt%, desorption/5.5 wt% H_2/0.01 bar/240 °C/5 min	39
14 wt% TiAl	Absorption/4 wt% H_2/1 bar/25 °C/100 min/max storage capacity: 5 wt%, desorption/4 wt% H_2/0.1 bar/240 °C/7 min	40
7 wt% $Mn_{3.6}Ti_{2.4}$	Absorption/5.3 wt% H_2/10 bar/275 °C/2 min, desorption/5.3 wt% H_2/0.02 bar/275 °C/8 min, cycle-life-time: 1400 h (1000 cycles)	41
10 wt% $ZrNi_5$	Absorption/5.3 wt% H_2/10 bar/275 °C/1 min, desorption/5.3 wt% H_2/0.02 bar/275 °C/12 min, cycle-life-time: 568 h (600 cycles)	42
10 wt% big-cube Zr_2Ni	Absorption/5.1 wt% H_2/10 bar/250 °C/100 s, desorption/5.1 wt% H_2/0.02 bar/250 °C/613 s, cycle-life-time: 1250 h (2546 cycles)	43

necessary to absorb 5.5 wt% H_2 within 10 min (Table 1). However, the dehydrogenation process of MgH_2/15 wt% $VNbO_5$ system when compared with our system, had taken place at a higher temperature (275 °C).

The MgH_2/10 wt% $V_{0.75}Ti_{0.05}Cr_{0.20}$ system can absorb 3 wt% H_2 at normal pressure and temperature within 75 min.[39] The dehydrogenation kinetics, however, showed that at 240 °C to 5.5 wt% was released in 5 min.[39] Better H_2 storage capacity (4 wt%) can be achieved within 100 min at normal pressure and temperature upon doping MgH_2 with 14 wt% titanium aluminide (TiAl) powders.[40] Likewise in the $MgH_2/V_{0.75}Ti_{0.05}Cr_{0.20}$ system, the dehydrogenation process required a longer time (7 min) and higher temperature (240 °C) to be complete.[40] In addition, some new systems such as $MgH_2/Mn_{3.6}Ti_{2.4}$, $MgH_2/ZrNi_5$ and MgH_2/big-cube Zr_2Ni[41–43] have shown promising results, indicated by fast uptake/release kinetics at moderate temperatures (250–275 °C), long cycle-life-time (600–2546 cycles), as shown in Table 1.

In contrast to pure metal catalysts, the catalytic agents presented in Table 1 are heterogeneous catalysts which do not react with Mg/MgH_2 to form intermediate compounds. Until now, the mechanism of this group of catalysts including MG-Ti_2Ni powders was not clear. It was agreed that doping MgH_2 with hard abrasive particles led to a dramatic disintegration of the MgH_2 powders to form finer powders.[32–43] They also play an important part in the splitting/recombination of hydrogen molecules during the hydrogenation/dehydrogenation processes.[41,42] This led to enhancement of the kinetics behavior of MgH_2 and lowering of the apparent activation energy.[37]

5. Conclusions

The synthesis of bulk nanocomposite MgH_2/10 wt% MG-Ti_2Ni strip, using cryo-milling combined with cold rolling techniques has been demonstrated. The as-prepared cold rolled strips consisted of ultrafine MgH_2 nano-lenses embedded in MG Ti_2Ni in a uniform fashion. The MgH_2 powder particles, which were immersed in a "pool" of hard amorphous-Ti_2Ni ultrafine powders, did not show a drastic growth in size during the kinetics measurements, and they maintained their characteristic nano-morphology. The chemical composition of the synthesized nanocomposite was homogeneous and did not reveal degradation/composition fluctuation beyond the nanoscale. This new MgH_2-based nanocomposite possessed excellent hydrogenation/dehydrogenation kinetics at a rather low

temperature and exhibited good cyclability. The results showed α-Ti_2Ni was neutral and did not undergo any reaction with the base material to form undesired phases, *e.g.*, TiH_2 and/or Mg_2NiH_4.

Conflicts of interest

There are no conflicts to declare.

Acknowledgements

Appreciation is extended to the Kuwait Foundation for the Advancement of Sciences (KFAS) for the partial financial support of this study related to Project EA061C under contract number: P315-35EC-01. The financial support received from the Kuwait Government through the Kuwait Institute for Scientific Research for purchasing the equipment used in the present work, using the budget dedicated for project P-KISR-06-04 led by the author in the Establishing Nanotechnology Center in KISR is highly appreciated.

Notes and references

1 M. Jefferson, *Renewable Energy*, 2006, **31**, 571–582.
2 L. Schlapbach and A. Zuttel, *Nature*, 2001, **414**, 353.
3 I. P. Jain, C. Lal and A. Jain, *Int. J. Hydrogen Energy*, 2010, **35**, 1121–1140.
4 A. Bocarsly and D. M. P. Mingos, *Fuel Cells and Hydrogen Storage*, Springer-Verlag Berlin Heidelberg, 1st edn, 2011, ch. 3.
5 G. Liu, Y. Wang, C. Xu, F. Qiu, C. An, L. Li, L. Jiao and H. Yuan, *Nanoscale*, 2013, **5**, 1074–1081.
6 A. Calka, *Appl. Phys. Lett.*, 1991, **59**, 1568–1570.
7 M. Sherif El-Eskandarany and A. Ashour, *J. Alloys Compd.*, 2000, **313**, 224–234.
8 Ki-J. Jeon, *et al.*,, *Nat. Mater.*, 2011, **10**, 286–290.
9 M. Sherif El-Eskandarany, *Sci. Rep.*, 2016, **6**, 26936, DOI: 10.1038/srep26936.
10 G. Principi, F. Agresti, A. Maddalena and R. Lo, *Energy*, 2009, **34**, 2087–2091.
11 J. Huot, *et al.*,, *Prog. Mater. Sci.*, 2013, **58**, 30–75.
12 C. Shang, M. Bououdina, Y. Song and Z. Guo, *Int. J. Hydrogen Energy*, 2004, **29**, 73–80.
13 G. Krishnan, *et al.*,, *Nanoscale*, 2018, **10**, 1297–1307.
14 C. Zhou, Z. Fang, C. Ren, J. Li and J. Lu, *J. Phys. Chem. C*, 2014, **118**, 11526–11535.
15 H. Simchi, A. Kaflou and A. Simchi, *Int. J. Hydrogen Energy*, 2009, **34**, 7724–7730.
16 Rafi-ud-din, Q. Xuanhui, L. Ping, L. Zhang, M. Ahmad, M. Zubair Iqbal, M. Yasir Rafique and M. Hassan Farooq, *RSC Adv.*, 2012, **2**, 4891–4903.
17 M. Sherif El-Eskandarany, E. Shaban and A. Alsairafi, *Energy*, 2016, **104**, 158–170.
18 H. Liu, *et al.*,, *J. Mater. Chem. A*, 2013, **1**, 12527–12535.
19 A. Bhatnagar, *et al.*,, *J. Mater. Chem. A*, 2016, **4**, 14761–14772.
20 N. A. Ali, *et al.*,, *RSC Adv.*, 2018, **8**, 15667–15674.
21 B. Li, Y. Liu, C. Li, M. Gao and H. Pan, *J. Mater. Chem. A*, 2014, **2**, 3155–3162.
22 S. Shinde, D.-H. Kim, Y. Jin-Young and J.-H. Lee, *Nanoscale*, 2017, **9**, 7094–7103.
23 R. A. Varin, T. Czujko and Z. Wronski, *Nanotechnology*, 2006, **17**, DOI: 10.1088/0957-4484/17/15/041.
24 M. Sherif El-Eskandarany, E. Shaban and B. Al-Halaili, *Int. J. Hydrogen Energy*, 2014, **39**, 12727–12740.
25 N. N. Sulaiman, N. Juahir, N. S. Mustafa, F. A. Halim and Y. M. Ismail, *J. Energy Chem.*, 2016, **25**, 832–839.
26 M. S. Yahya and M. Ismail, *J. Energy Chem.*, 2017, DOI: 10.1016/j.jechem.2017.10.
27 X. Xiao, Z. Liu, S. Saremi-Yarahmadi and D. H. Gregory, *Phys. Chem. Chem. Phys.*, 2016, **18**, 10492–10498.
28 X. Huang, *Materials*, 2009, **2**, 2369–2403.
29 F. Cuevas, D. Korablov and M. Latroche, *Phys. Chem. Chem. Phys.*, 2012, **14**, 1200–1211.
30 A. Valentoni, G. Mulas, S. Enzo and S. Garroni, *Phys. Chem. Chem. Phys.*, 2018, **20**, 4100–4108.
31 P. Vajeeston, P. Ravindran, A. Kjekshus and H. Fjellvåg, *Phys. Rev. Lett.*, 2002, **89**, 175506–175509.
32 K.-F. Aguey-Zinsou, J. R. Ares Fernandez, T. Klassen and R. Bormann, *J. Hydrogen Energy*, 2007, **32**, 2400–2407.
33 N. Hanada, T. Ichikawa, S. Hino and H. Fujii, *J. Alloys Compd.*, 2006, **420**, 46–49.
34 M. Sherif El-Eskandarany, E. Shaban and A. Al-Shemmiri, *Int. J. Hydrogen Energy*, 2014, **39**, 21097–21106.
35 K. S. Jung, E. Y. Lee and K. S. Lee, *J. Alloys Compd.*, 2006, **421**, 179–184.
36 I.-H. Kwon, J.-L. Bobet, J.-S. Bae and M.-Y. Song, *J. Alloys Compd.*, 2005, **396**, 264–268.
37 A. Valentoni, G. Mulas, S. Enzo and S. Garroni, *Phys. Chem. Chem. Phys.*, 2018, **20**, 4100–4108.
38 A. Ranjbara, Z. P. Guoa, X. B. Yua, D. Wexler, A. Calka, C. J. Kimd and H. K. Liu, *Mater. Chem. Phys.*, 2009, **114**, 168–172.
39 C. Ren, Z. Z. Fang, C. Zhou, J. Lu, Y. Ren and X. Zhang, *J. Phys. Chem. C*, 2014, **118**, 21784.
40 C. Zhou, Z. Z. Fang, C. Ren, J. Li and J. Lu, *J. Phys. Chem. C*, 2013, **117**, 12973–12980.
41 M. Sherif El-Eskandarany, H. Al-Matrouk and E. Shaban, *Int. J. Hydrogen Energy*, 2015, **40**, 10139–10149.
42 M. Sherif El-Eskandarany, E. Shaban, H. Al-Matrouk, M. Behbehani, A. Alkandary, F. Aldakheel, *et al.*,, *Materials Today Energy*, 2017, **3**, 60–71.
43 M. Sherif El-Eskandarany, H. Al-Matrouk, E. Shaban and A. Al-Duweesh, *Energy*, 2015, **91**, 274–282.

